Soil Dynamics and Earthquake Engineering 124 (2019) 121–135

Contents lists available at ScienceDirect

Soil Dynamics and Earthquake Engineering

journal homepage: www.elsevier.com/locate/soildyn

A novel semi-micro multilaminate elasto-plastic model for the liquefaction of sand

Hadi Dashti[a,*], Seyed Amirodin Sadrnejad[b], Navid Ganjian[a]

[a] Department of Civil Engineering, Science and Research Branch, Islamic Azad University, Tehran, Iran
[b] Department of Civil Engineering, K.N. Toosi University of Technology, Tehran, Iran

ARTICLE INFO

Keywords:
Granular material
Constitutive law
Micro plane
Induced anisotropy
Cyclic mobility

ABSTRACT

After the liquefaction of sand, the prediction of anisotropy and heterogeneity is one of the complexities of constitutive law. This study aimed to develop a method to more effectively assess anisotropy and strain and stress distributions, and determine their history in cohesionless soil. To achieve this objective, instead of defining all the direction-dependent events on the three orthogonal planes of the Cartesian coordinate system, numerical integration was utilized to make use of 17 planes with pre-defined directions. This leads to a more accurate and powerful assessment of anisotropy and its effects. The constitutive equations of the proposed model were adjusted with a multilaminate framework, and its result for different monotonic and cyclic loading, drained and undrained conditions, and different pressures and void ratios were verified using the experimental data. Finally, the model's performance in predicting induced anisotropy is demonstrated under cyclic mobility conditions on the 17 planes.

1. Introduction

The constitutive characteristics of sand as a basic geomaterial have a significant effect on its applications. Developing a constitutive model for sand, and especially its liquefaction, is a challenging task. Under monotonic or cyclic loading conditions, sandy soils tend to exhibit dilatancy. In undrained conditions, this behavior leads to increased pore pressure and decreased effective stress, and this reduction can sometimes lead to liquefaction.

Another important parameter that can affect soil liquefaction resistance under cyclic loads is inherent and induced anisotropy due to plastic deformation, which can be defined as the properties of soil fabric. Some studies have tried to establish a relationship between the important microscopic and macroscopic properties of sand, and incorporate the result into their constitutive models [1,2]. There are essentially two types of anisotropy in granular material, inherent anisotropy and induced anisotropy. Inherent anisotropy is created during the sedimentation of geomaterials as a result of the placement of the soil particles, the void ratio, and the inter-particle contact [3,4]. Inherent anisotropy remains unchanged as long as the material is in its elastic state. Induced anisotropy occurs under the influence of plastic strain and loading history, and it plays a significant role in the mechanical behavior of granular soils [2,5]. Unlike inherent anisotropy, induced anisotropy evolves with plastic deformation over the course of the loading process. While many studies have examined soil anisotropy, the development of anisotropy during liquefaction and the ensuing effects, including changes in effective stress and soil stiffness, are still under debate. Anisotropy in granular soils subjected to cyclic or monotonic loading has also been extensively studied [6–10]. Some researchers have studied the inter-particle contact level and have also predicted the effects of anisotropy on the behavior of granular soil using micromechanical models, such as the discrete element model [11–17].

Researchers have proposed various constitutive models to predict the behavior of sandy soils under monotonic or cyclic loading conditions [1,6,18–23]. Some of these models have restrictions regarding the type of load, but there also a number of comprehensive models that can simulate the experimental results for different loads and drained and undrained conditions [24,25]. One of the leading models for predicting the effects of anisotropy is the one proposed by Dafalias and Manzari [24]. The original form of this model was first introduced by Manzari and Dafalias [26] based on hypo-plasticity theory [27,28]. Later, other researchers developed this model for different conditions [24,29,30].

Some researchers have modeled full anisotropy using the multilaminate framework, and for various materials, including soil [31–33], and in damage models developed for concrete [34–36]. In concrete, this model is sometimes also known as a microplane model [37,38]. The multilaminate framework is a powerful method for predicting the anisotropic behavior of material based on the separation of behavior on

* Corresponding author.
E-mail addresses: hdashti1356@yahoo.com (H. Dashti), sadrnejad@kntu.ac.ir (S.A. Sadrnejad), n.ganjian@srbiau.ac.ir (N. Ganjian).

https://doi.org/10.1016/j.soildyn.2019.05.031
Received 17 July 2017; Received in revised form 17 May 2018; Accepted 18 May 2019

multiple so-called integration (or sample) planes. This framework allows the stress-strain behavior to be approximated using different elasto-plastic or elasto-viscoplastic theories, and it allows the constitutive effects, such as softening, hardening, etc., to be modeled for different loading conditions. The characteristics of these theories and the multilaminate framework enable researchers to predict the inherent and induced anisotropy of a material, the effects of rotation of the principal stress and strain axes during nonlinear behavior, the non-coaxiality effects of the principal stress and strain axes, and the strain concentration. In addition, the resulting model can incorporate the effects of other complex constitutive factors. Another important feature of multilaminate models is their ability to analyze the behavior along specific directions. The presence of joints in rock and the status of the bedding plane in sediments, as well as other phenomena, can cause the material to exhibit different behavioral characteristics along different directions. The multilaminate model allows the behavior, and thus factors, such as damage, fatigue, and creep, to be determined along different directions [39].

The present study develops the model reported by Dafalias and Manzari [24] with the multilaminate framework for monotonic and cyclic loading and drained and undrained conditions. The constitutive law equation is first presented and explained, after which the effects of the constant model on the planes are investigated, and calibrated values are obtained. The derived results are then compared with the experimental data, and standard triaxial tests are conducted to determine the proposed model's effectiveness. Finally, the applicability of the model under initial shear stress in soil under cyclic loading conditions and its performance in predicting induced anisotropy are evaluated on the 17 planes.

2. Multilaminate theory

The section presents a discussion of the principles of the mutilaminate model [39].

2.1. Multilaminate model

The multilaminate theory addresses the numerical relationship between the inter-particle behavior (micro behavior) and the mechanical properties (macro behavior) of materials in the form of a constitutive equation. In other words, the multilaminate model derives the material properties from the attributes of its constituent elements, and it allows the stress-strain behavior to be determined based on the inter-particle behavior. As we know, materials are made of an unlimited number of solid particles (crystals or grains), and surface contacts and interactions are induced by the forces that act on their contact surfaces. Proper analysis of the behavior of particles and their contact surface depends on an accurate analysis of the number, size, shape, roughness, and particle resistance at these surfaces. Consequently, this approach to granular materials is more complex than the approach in which the medium is assumed to be continuous. For simplicity's sake, the behavior of these materials can be assumed to be the combined effect of the elastic behavior of the grains and the plastic slip at their surfaces. Thus, the three-dimensional (3D) behavior of materials can be expressed by integrating the effects of the numerous sample planes on which the slip occurs. Therefore, the soil mass is divided into multiple adjacent polyhedral blocks. As with actual grains, in these models, slip and deformation along the direction normal to the contact surfaces of the block operate as the principal mechanism of plastic strain.

2.2. Assumptions

A polyhedral block subjected to small shear stress undergoes elastic shear deformation, but when this stress increases beyond a certain point, the polyhedral blocks start to slide along their bounding surface, or the so-called slip plane. As the deformation increases, the shear stress required to cause further deformation also increases. At any time, the total shear deformation is the sum of the elastic shear deformation of the polyhedral blocks and the plastic shear deformation caused by the adjacent blocks sliding over each other. As stress decreases, elastic components return to the beginning of the deformation path, and, after a certain point, the polyhedral blocks start to slide in the opposite direction. The shear stress required for sliding depends on the vertical stress, and the sliding occurs only when the stress surpasses the yield limit. Furthermore, the sliding occurs only along the slip planes, as shown in Fig. 1. On this basis, the greater the number and the extent of the defined planes, the more realistic will be the sliding and opening-closing of the planes. Consequently, when a material tends to deform in a particular direction along which no plane is defined, deformation will occur in the two planes that are near that direction. This simulation allows researchers to obtain the specific internal deformation mechanism that is closest to reality based on numerical approximation.

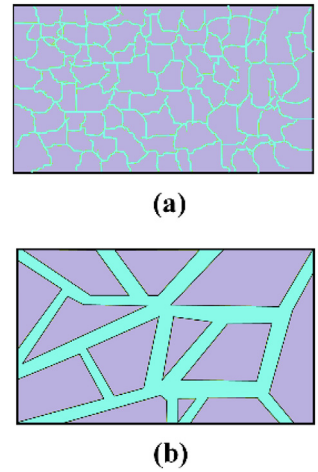

Fig. 1. a) schematic of actual particle aggregation; b) two-dimensional (2D) schematic of the assembly of the artificial polyhedral blocks.

2.3. Numerical concept of the multilaminate theory

In the multilaminate theory, the calculations are based on the numerical integration of a mathematical function over the surface of a unit sphere. This mathematical function must be able to express the changes in the physical properties over the surface of the sphere. During numerical integration, the surface of a hypothetical unit sphere can be approximated with a multitude of flat planes that are tangent to different parts of the surface (Fig. 2). Thus, each of these planes has a single point of contact with the surface of the sphere, and the number of these contacts or reference points can be defined by adjusting these

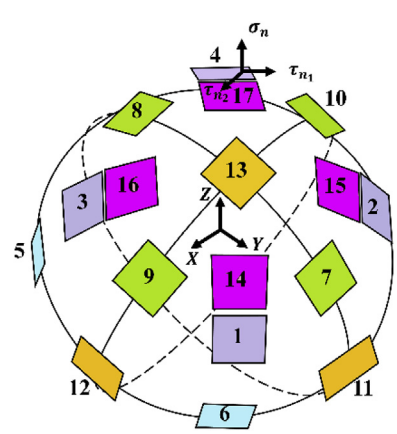

Fig. 2. Position of the 17 sample planes on the sphere.

planes. During numerical integration, the value of the parameter defined over the sphere's surface can be obtained at the mentioned points. Numerical integration of the continuous function f (x, y, z) over the surface of a sphere can be obtained by the sum of the values of f (x, y, z) in the sample points multiplied by their corresponding weight coefficients. Errors can be reduced by increasing the number of sample points. In this case, it is proved that the use of 26 sample points reduces the error by the order of six. The following equation expresses the relationship between normal integration and numerical integration:

$$\iint_{\Omega} f(x, y, z)dxdydz = 4\pi \sum_{i=1}^{n} w(i) f(x_i, y_i, z_i) \tag{1}$$

Ω = area of the sphere
n = number of points
w(i) = weight coefficient of point i
f_i (x_i, y_i, z_i) = value of the function f at the point i

On this basis, assuming a formulation for sliding and opening-closing in each plane, the internal mechanism of the motion of the material at a point can be expressed as the sum of the sliding and opening-closing, and the overall motion or deformation effect at that point can, therefore, be obtained by performing an integral summation. Thus, the function f_i (x_i, y_i, z_i), which represents deformation over each plane, needs to be assigned a formulation. Therefore, the overall deformation at a certain point of the material will depend on the formula and the shape of the stress-strain curve over the defined reference planes. Next, nonlinear constitutive equations must be defined differentially on the planes to allow the behavior of the materials to be predicted through integration.

Given the weakness of the 13-plane model, due to its inability to provide the integrated effects, in some of the strain paths, minimal extension of strain distribution occurs on the surface of the sphere and some of the strain distribution information can be lost. This problem, i.e., the failure to satisfy the compatibility constraints of the strains and deformations, can be solved by adjusting the number of planes. To do so, as a basic condition, after transferring every stress and strain tensor component from the global coordinate system to the coordinate system of the planes, the strain and stress must be calculated, and, when transferring the calculated strains or stresses back to the original system, there should be no difference in the behavioral outputs. Transfer of stress and strain tensors to the new coordinate system defined for 13 planes must be performed using the three orthogonal coordinate planes defined for those systems. This means that, in order to perform the coordinate transfer for 13 planes, one must define a total of 13 × 3 = 39 coordinate planes. However, some of these 39 planes are duplicates, which can be easily identified and eliminated. Careful elimination of the duplicate planes results in a total of 34 micro-planes on the sphere surface, or 17 micro-planes on the hemisphere (given the symmetry of the center). To better illustrate the geometry of the extra planes in this model, tangential planes equivalent to the micro-planes on the unit sphere are depicted. Fig. 3 shows the position of these planes inside the unit cube and Table 1 provides the direction cosines (normal stress), direction of the shear stresses, $\tau_{n1}$and τ_{n2} , and the weight coefficients of the 17 planes.

Assuming that l, m, and n are the directions of the cosines normal to the plane, that l', m', and n' are the directions of the cosines of the shear stress τ_{n_1}, and that l", m", and n" are the directions of the cosines of the shear stress τ_{n_2}, according to the results of Sadrnejad and Labibzade [36] and using matrix algebra relations, the value of the stress in the plane, in terms of the stress at the point, can be obtained from the following equation:

$$\boldsymbol{\sigma}_{Plane} = \begin{bmatrix} \sigma_n \\ \tau_{n_1} \\ \tau_{n_2} \end{bmatrix} = \begin{bmatrix} l & m & n \\ l' & m' & n' \\ l'' & m'' & n'' \end{bmatrix} \begin{bmatrix} \sigma_{xx} & \tau_{xy} & \tau_{xz} \\ \tau_{yx} & \sigma_{yy} & \tau_{yz} \\ \tau_{zx} & \tau_{zy} & \sigma_{zz} \end{bmatrix} \begin{bmatrix} l \\ m \\ n \end{bmatrix} \tag{2}$$

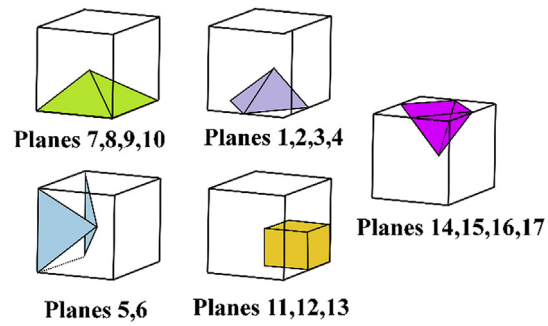

Fig. 3. Direction of the 17 planes in the center of the cube.

where σ_n is the stress normal to the plane, τ_{n_1} and τ_{n_2} are the shear stress along plane 1 and plane 2, σ_{xx}, σ_{yy}, and σ_{zz} are the normal stresses at the point, and τ_{xy}, τ_{xz}, τ_{yz}, τ_{yx}, τ_{zx}, and τ_{zy} are the shear stresses at the point. In this present study, body forces are assumed to be absent; thus, $\tau_{xy} = \tau_{yx}$, $\tau_{xz} = \tau_{zx}$, and $\tau_{yz} = \tau_{zy}$.

After calculating the stress on the planes, the elastic and plastic strains on the planes are calculated, and the resulting strains are transferred to the point using the following equation. This equation is equivalent to the plane-point stress transfer equation proposed by Sadrnejad and Labibzade [36]:

$$\varepsilon_{ij} = 6 \times \sum_{n=1}^{17} w(n)[\boldsymbol{T}_P(n)][\varepsilon_{Plane}(n)] \tag{3}$$

In the above equation, ε_{ij} is the six component strain at the point:

$$\varepsilon_{ij} = \begin{Bmatrix} \varepsilon_{xx} \\ \varepsilon_{yy} \\ \varepsilon_{zz} \\ \gamma_{xy} \\ \gamma_{yz} \\ \gamma_{xz} \end{Bmatrix} \tag{4}$$

$\boldsymbol{T}_P(n)$ is the plane transfer matrix. The value of $\boldsymbol{T}_P(n)$ of each plane is calculated using the following equation:

$$\boldsymbol{T}_P(n) = \begin{bmatrix} l^2 & ll' & l''l \\ m^2 & m'm & m''m \\ n^2 & n'n & n''n \\ lm & 1/2(l'm + m'l) & 1/2(m''l + l''m) \\ mn & 1/2(m'n + n'm) & 1/2(m''n + n''m) \\ ln & 1/2(l'n + n'l) & 1/2(l''n + n''l) \end{bmatrix} \tag{5}$$

$\varepsilon_{Plane}(n)$ is the strain equivalent to the stress in the planes and $w(n)$ is the weight coefficient of the planes.

3. Constitutive law on the planes

Among the various models that can be used to express sand behavior in soil liquefaction, the model reported by Dafalias and Manzari [24] is useful. This model is compatible with the principles of soil mechanics, the definition of bounding surface, the dilatancy of the surface, and its dependence on the state parameter and its changes during loading; thus, its ability to match these with the critical surface in the failure conditions leads to the correct prediction of the expansion and contraction behavior of dense and loose sand and the softening property of the material. In addition, adding the fabric-related parameters to the model of sandy soils has led to better agreement of their inverse loading results with experimental observations. Given these features, and to improve the performance of this model for different loading conditions, we use it as the constitutive model for the 17 planes in the multilaminate model.

The following sections describe the governing equations of the

Table 1
Direction of the cosines, τ_{n1} , τ_{n2} , in the 17 planes and the weight coefficients of the 17 planes.

plane(i)	l	m	n	l'	m'	n'	l"	m"	n"	w(i)
1	0.57735	0.57735	0.57735	0.70711	−0.7071	0	0.40825	0.40825	−0.8165	0.0203
2	0.57735	−0.5774	0.57735	0.70711	0.70711	0	0.40825	−0.40825	−0.8165	0.0203
3	−0.5774	0.57735	0.57735	0.70711	0.70711	0	0.40825	−0.40825	0.8165	0.0203
4	−0.5774	−0.5774	0.57735	0.70711	−0.7071	0	0.40825	0.40825	0.8165	0.0203
5	0.70711	0.70711	0	0.70711	−0.7071	0	0	0	1	0.0581
6	−0.7071	0.70711	0	0.70711	0.70711	0	0	0	1	0.0581
7	0.70711	0	0.70711	0	1	0	0.70711	0	−0.70711	0.0301
8	−0.7071	0	0.70711	0	1	0	−0.7071	0	−0.70711	0.0301
9	0	−0.7071	0.70711	1	0	0	0	0.70711	0.70711	0.0301
10	0	0.70711	0.70711	1	0	0	0	−0.70711	0.70711	0.0301
11	1	0	0	0	1	0	0	0	1	0.0383
12	0	1	0	1	0	0	0	0	1	0.0383
13	0	0	1	0	1	0	1	0	0	0.0203
14	0.40825	0.40825	0.8165	0.70711	−0.7071	0	0.57735	0.57735	−0.57735	0.0191
15	0.40825	−0.4082	0.8165	0.70711	0.70711	0	0.57735	−0.57735	−0.57735	0.0191
16	−0.4082	0.40825	0.8165	0.70711	0.70711	0	0.57735	−0.57735	0.57735	0.0191
17	−0.4082	−0.4082	0.8165	0.70711	−0.7071	0	0.57735	0.57735	0.57735	0.0191

planes, which are based on the equations used by Dafalias and Manzari [24]. It should be noted that, in all the equations, the subscript "P" refers to the plane and the bold letters indicate tensor variables.

3.1. Model of elastic behavior in the plane

In the hypo-elastic theory, G_{Plane} and K_{Plane} are defined as a function of the void ratio e and the stress normal to the plane σ_n:

$$G_{Plane} = G_{0P} P_{atm} (2.97 - e)^2/(1 + e)\left(\frac{\sigma_n}{P_{atm}}\right)^{1/2} \tag{6}$$

and

$$K_{Plane} = \frac{2(1 + \upsilon_P)}{3(1 - 2\upsilon_P)} G_{Plane} \tag{7}$$

where G_{Plane} is the elastic shear modulus of the soil, $K_{Plane}$is the elastic bulk modulus of the soil, υ_P is the Poisson's ratio of the soil on the plane, G_{0P} is model constant of the plane, and P_{atm} is the atmospheric pressure.

3.2. Critical state line

This multilaminate model utilizes the critical state theory proposed in for the planes. In the theory, the critical void ratio $e_{c(Plane)}$ and normal stress σ_n of the planes are linked through the following equation:

$$e_{c(Plane)} = e_{0P} - \lambda_{cP}\left(\sigma_n / P_{atm}\right)^{\xi_P} \tag{8}$$

where e_{0P} and λ_{cP} are the model constants for the plane. The state parameter ψ_P is defined as follows:

$$\psi_{Plane} = e_{Plane} - e_{c(Plane)} \tag{9}$$

where e_{Plane} is the void ratio in the plane. ψ_{Plane} is used to define the bounding surface, the dilatancy surface, and the critical surface, which all vary with variations in this parameter during loading. This dependency allows one to predict some sand features, such as softening or the dilatancy phase change, and the model's compliance with the theory of limit states.

3.3. Yield surface

The function of yield surface in the plane is defined by the following equation:

$$f_{Plane} = [(\boldsymbol{S}_{Plane} - \sigma_n \boldsymbol{\alpha}_{Plane}) : (\boldsymbol{S}_{Plane} - \sigma_n \boldsymbol{\alpha}_{Plane})]^{1/2} - \sqrt{2/3}\, \sigma_n m_P = 0 \tag{10}$$

In this equation, tensor $\boldsymbol{S}_{Plane}$ is defined as follows:

$$\boldsymbol{S}_{Plane} = \boldsymbol{\sigma}_{Plane} - \sigma_n \boldsymbol{I}_{\text{Plane}} \tag{11}$$

where:

$$\boldsymbol{I}_{\text{Plane}} = \begin{bmatrix} 1 & 0 & 0 \\ 0 & 0 & 0 \\ 0 & 0 & 0 \end{bmatrix} \tag{12}$$

Also, $\boldsymbol{r}_{Plane}$ is defined as follows:

$$\boldsymbol{r}_{Plane} = \frac{\boldsymbol{S}_{Plane}}{\sigma_n} \tag{13}$$

and $\boldsymbol{\alpha}_{Plane}$ is the deviatoric back stress ratio tensor, which is used to determine the axis of the yield surface. The symbol,:, refers to the multiplication of two tensors, i.e., $a : b = tr(ab)$. The equation of the f_{plane} expresses the cone geometry in the space of the axes σ_n , τ_{n_1}, and τ_{n_2}. m_P is a constant of the model. Fig. 4 shows a schematic illustration for yield surface, bounding surface, dilatancy surface, and critical surface at the point and in the spaces of σ_n , τ_{n_1} and τ_{n_2} on the plane.

Based on the equation of the f_{Plane}, slope of the yield surface, $\boldsymbol{r}_{Plane}$ is obtained as follows:

$$\boldsymbol{L}_{Plane} = \partial f_{Plane} / \partial \boldsymbol{\sigma}_{Plane} \tag{14}$$

The vector $\boldsymbol{n}_{Plane}$, which is the unit vector normal to the yield surface in the deviatoric stress space, is defined as follows:

$$\boldsymbol{n}_{Plane} = \frac{\boldsymbol{r}_{Plane} - \boldsymbol{\alpha}_{Plane}}{\|\boldsymbol{r}_{Plane} - \boldsymbol{\alpha}_{Plane}\|} \tag{15}$$

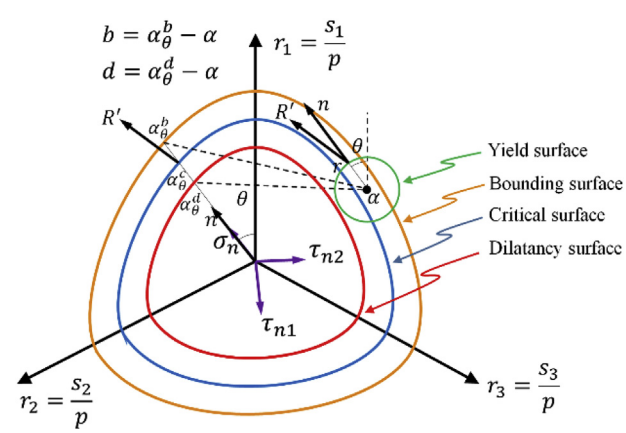

Fig. 4. Schematic view of yield surface, bounding, dilatancy and critical surface at the point and view of σ_n, τ_{n_1},and τ_{n_2}on the plane.

where ‖ ‖ represents the tensor norm.

3.4. Evolution of the plastic strain

The increment of the plastic strain is depicted in the following equation:

$$d\boldsymbol{\varepsilon}^{P}_{Plane} = < L > \boldsymbol{R}_{Plane} \tag{16}$$

Where L is the loading index (or the plastic factor), $< \ >$ are the Macaulay brackets, and $<x>$ equals x if $x > 0$ and $<x>$ equals zero if $x \leq 0$. $\boldsymbol{R}_{Plane}$is the direction of the vector $d\varepsilon^{P}_{Plane}$. In this model, in general, $\boldsymbol{R}_{Plane} \neq {}^{\partial f_{Plane}}/_{\partial \sigma_{Plane}}$. Thus, it is assumed that plasticity is governed by the non-associated flow rule. The following equation divides the R_{Plane} into the deviatoric and volumetric components:

$$\boldsymbol{R}_{Plane} = \boldsymbol{R}'_{Plane} + {}^{1}/_{3} D_{Plane} \boldsymbol{I}_{Plane} = B_{Plane} \boldsymbol{n}_{Plane} + C_{Plane}\left(\boldsymbol{n}^{2}_{Plane} - {}^{1}/_{3}\boldsymbol{I}_{Plane}\right) + {}^{1}/_{3} D_{Plane} \boldsymbol{I}_{Plane} \tag{17}$$

D_{Plane} is a scalar value that is related to dilatancy, and B_{Plane} and C_{Plane} are used to examine the effect of the Lode angle on the direction of the plastic strain increment; these two parameters are expressed as follows:

$$B_{Plane} = 1 + \frac{3}{2} \times \frac{(1 - C_P)}{C_P} \times g_{Plane} \times cos3\theta_{Plane} \tag{18}$$

$$C_{Plane} = 3\sqrt{3/2} \times \frac{(1 - C_P)}{C_P} \times g_{Plane} \tag{19}$$

C_P is the constant of the plane and θ_{Plane} is the effect of Lode's angle in the plane, which are defined as follows:

$$cos3\theta_{Plane} = \sqrt{6}\, trc\ \boldsymbol{n}^{3}_{Plane} \tag{20}$$

g_{Plane} is the interpolation function that is used to determine the bounding, dilatancy, and critical surfaces in different stress paths, and is defined as follows:

$$g_{Plane} = \frac{2C_P}{(1 + C_P) - (1 - C_P)cos3\theta_{Plane}} \tag{21}$$

The dilatancy parameter for $D_{Plane}$is defined with the following equation:

$$D_{Plane} = A_{d(Plane)}(\boldsymbol{\alpha}^{d}_{\theta(Plane)} - \boldsymbol{\alpha}_{Plane}):\ \boldsymbol{n}_{Plane} \tag{22}$$

The bounding surface of the dilatancy state and $A_{d(Plane)}$are defined by the following equations:

$$\boldsymbol{\alpha}^{d}_{\theta(Plane)} = \sqrt{2/3} \times [g_{Plane} \times M_P \times \exp(n^{d}_{P} \times \psi_{Plane}) - m_P]\boldsymbol{n}_{Plane} \tag{23}$$

and:

$$A_{d(Plane)} = A_{0P}(1 + < \boldsymbol{Z}_{Plane}: \boldsymbol{n}_{Plane} >) \tag{24}$$

where n^{d}_{P} , m_P , and A_{0P} are the model constants for the plane. The fabric dilatancy tensor rate in the planes $d\boldsymbol{Z}_{Plane}$ is calculated as follows:

$$d\boldsymbol{Z}_{Plane} = -C_{ZP} < - d\varepsilon^{P}_{VPlane} > (Z_{maxP}\boldsymbol{n}_{Plane} + \boldsymbol{Z}_{Plane}) \tag{25}$$

where C_{ZP} and Z_{maxP} are the model constants for the planes, and $d\varepsilon^{P}_{VPlane}$ is the volumetric plastic strain rate in the plane, which is calculated using the following equation:

$$d\varepsilon^{P}_{VPlane} = < L_{Plane} > D_{Plane} \tag{26}$$

The rate of deviatoric back stress ratio tensor can be obtained from the following equation:

$$d\boldsymbol{\alpha}_{Plane} = < L_{Plane} > 2/3 h_{Plane}(\boldsymbol{\alpha}^{b}_{\theta(Plane)} - \boldsymbol{\alpha}_{Plane}) \tag{27}$$

where $\boldsymbol{\alpha}^{b}_{\theta(Plane)}$ and h_{Plane} can be calculated using the following equation:

$$\boldsymbol{\alpha}^{b}_{\theta(Plane)} = \sqrt{2/3} \times [g_{Plane} \times M_P \times \exp(-n^{b}_{P} \times \psi_{Plane}) - m_P]\boldsymbol{n}_{Plane} \tag{28}$$

and

$$h_{Plane} = \frac{b_{0(Plane)}}{(\boldsymbol{\alpha}_{Plane} - \boldsymbol{\alpha}_{ini(Plane)}):\ \boldsymbol{n}_{Plane}} \tag{29}$$

The coefficient $b_{0(Plane)}$ is calculated using the following equation:

$$b_{0(Plane)} = G_{0P} h_{0P}(1 - C_{hp} e)\left(\frac{\sigma_n}{P_{atm}}\right)^{-1/2} \tag{30}$$

In this equation, C_{hp}, h_{0P}, and G_{0P} are the model constants for the planes, and $\boldsymbol{\alpha}_{ini(Plane)}$ is the initial value of $\boldsymbol{\alpha}_{Plane}$ at the start of each loading and unloading step. Based on the mathematical calculations, the loading index L can be obtained from the following equation:

$$L_{Plane} = \frac{(2 \times G_{Plane}\boldsymbol{n}_{Plane}: d\boldsymbol{e}_{Plane} - \boldsymbol{n}_{Plane}: \boldsymbol{r}_{Plane} d\varepsilon_{VPlane} \times K_{Plane})}{(K_{P(Plane)} + 2G_{Plane}(B_{Plane} + C_{Plane} tr\boldsymbol{n}^{3}_{Plane}) - K_{Plane} D_{Plane}\boldsymbol{n}_{Plane}: \boldsymbol{r}_{Plane})} \tag{31}$$

where the plastic modulus $K_{P(Plane)}$ is calculated using the following equation:

$$K_{P(Plane)} = 2/3 \times \sigma_n \times h_{Plane}(\boldsymbol{\alpha}^{b}_{\theta(Plane)} - \boldsymbol{\alpha}_{Plane}):\ \boldsymbol{n}_{Plane} \tag{32}$$

Finally, given that the incremental volumetric strain of $d\varepsilon_{VPlane}$ and the incremental deviatoric strain of $d\boldsymbol{e}_{Plane}$ constitute the sum of their elastic and plastic components, $d\varepsilon_{VPlane} = d\varepsilon^{e}_{VPlane} + d\varepsilon^{P}_{VPlane}$ and $d\boldsymbol{e}_{Plane} = d\boldsymbol{e}^{e}_{Plane} + d\boldsymbol{e}^{P}_{Plane}$, the stress increment in plane $d\boldsymbol{\sigma}_{Plane}$ is calculated as follows:

$$d\boldsymbol{\sigma}_{Plane} = 2G_{Plane}\, d\boldsymbol{e}^{e}_{Plane} + K_{Plane} d\varepsilon_{VPlane}\boldsymbol{I}_{\mathrm{Plane}} - < L > \left\{2G_{Plane}\left[B_{Plane}\boldsymbol{n}_{Plane} + C_{Plane}\left(\boldsymbol{n}^{2}_{Plane} - {}^{1}/_{3}\boldsymbol{I}_{\mathrm{Plane}}\right)\right] + K_{Plane} D_{Plane}\boldsymbol{I}_{\mathrm{Plane}}\right\} \tag{33}$$

where elastic deviatoric strain $d\boldsymbol{e}^{e}_{Plane}$ is calculated thus:

$$d\boldsymbol{e}^{e}_{Plane} = \frac{d\boldsymbol{S}_{Plane}}{(2 * G_{Plane})} \tag{34}$$

3.5. The undrained condition

In this multilaminate model, excess pore pressure is calculated using the Naylor theory [40,41]. According to this theory, the bulk modulus of water/soil composite K_u can be calculated using the following equation:

$$\frac{1}{K_u} = \frac{(1 - n)}{K_S} + \frac{n}{K_W} \tag{35}$$

where n is the porosity of the soil, K_W is the bulk modulus of the water, and K_S is the bulk modulus of the solid portion of the soil. Incremental pore water pressure can be calculated using the following equation:

$$\delta\boldsymbol{u} = K_u \boldsymbol{m}^T \delta\varepsilon_V \tag{36}$$

Where

$$\boldsymbol{m}^T = [1\ 1\ 1\ 0\ 0\ 0] \tag{37}$$

and $\delta\varepsilon_V$ is the incremental volumetric strain. Finally, the incremental stress $\delta\boldsymbol{\sigma}$, in terms of incremental effective stress $\delta\boldsymbol{\sigma}'$, is obtained from the following equation:

$$\delta\boldsymbol{\sigma} = \delta\boldsymbol{\sigma}' + m\delta\boldsymbol{u} \tag{38}$$

4. Determination of the model constants

In previous studies, the constants of the Dafalias-Manzari model have been derived from the experimental plots relating to Toyoura sand [26,42]. Considering the lack of access to tests conducted on the 17 planes, all the planes are assumed to have identical constants. These

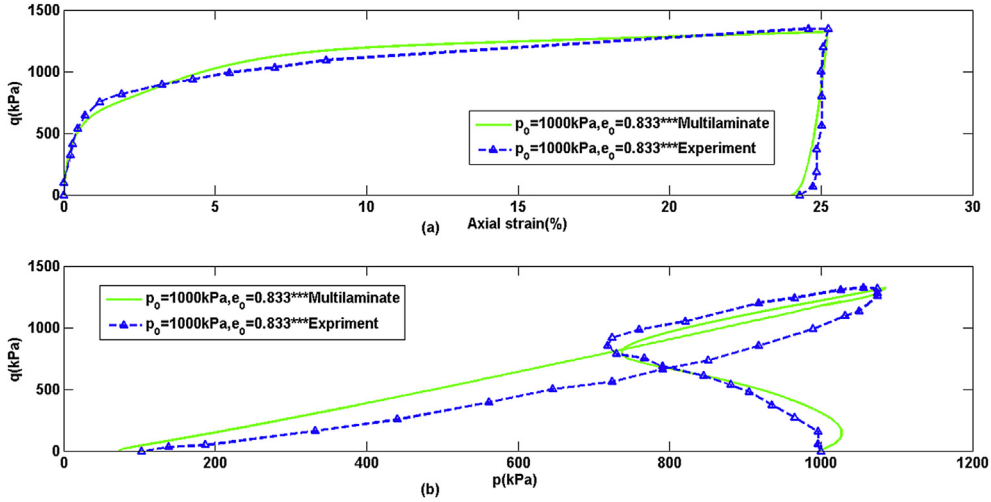

Fig. 5. Calibration of the numerical model with the experimental results for monotonic loading and unloading conditions in the standard triaxial test with $p_0 = 1000\ kPa$ and $e_0 = 0.833$; a) axial strain versus deviatoric stress; b) confining pressure versus deviatoric stress.

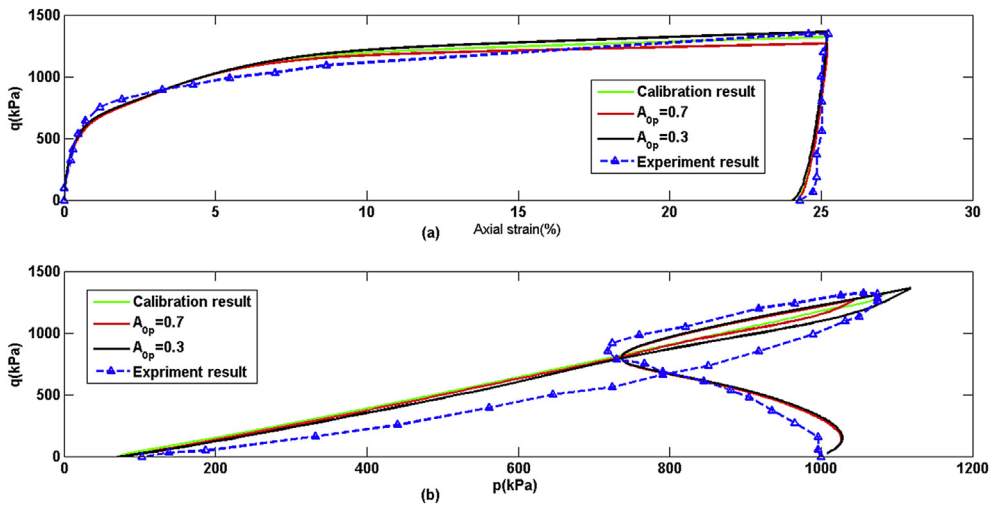

Fig. 6. The effects of constant A_{0P} on the curves of the axial strain-deviatoric stress (a) and the confining pressure-deviatoric stress (b).

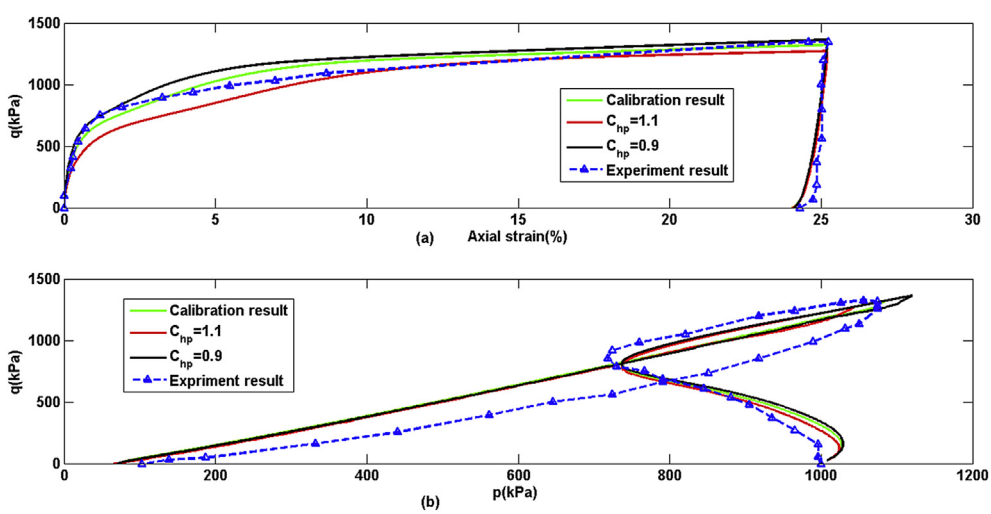

Fig. 7. The effects of constant C_{hP} on the curves of the axial strain-deviatoric stress (a) and the confining pressure-deviatoric stress (b).

constants are determined using a sensitivity analysis, the results of which are presented in Figs. 6–20. Each of the model constants has a certain task regarding the agreement of the numerical and experimental results. Some of the constants, namely, m_P, M_P, C_{hP}, C_P, and h_{0P}, are more effective in terms of loading and unloading on the curves of deviatoric stress versus axial strain as the p-q curves appropriately

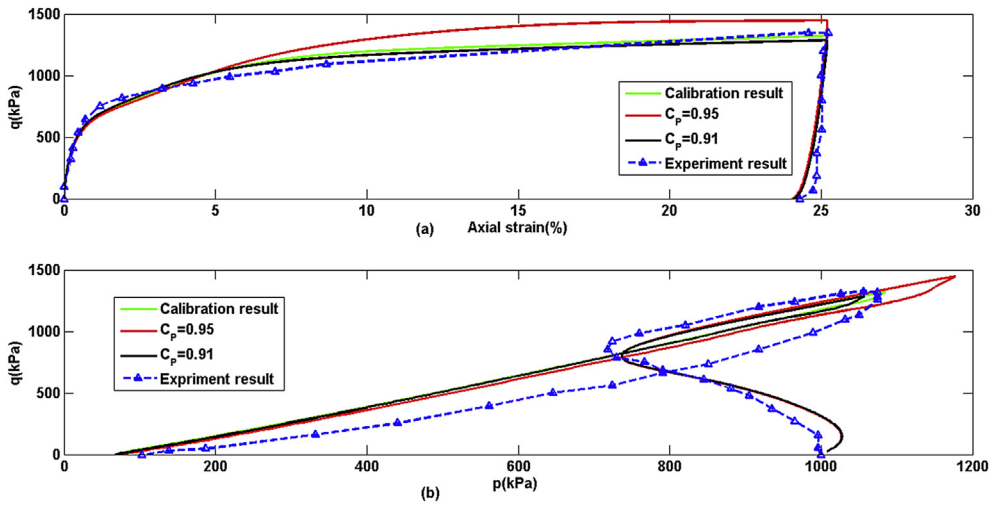

Fig. 8. The effects of constant C_P on the curves of the axial strain-deviatoric stress (a) and the confining pressure-deviatoric stress (b).

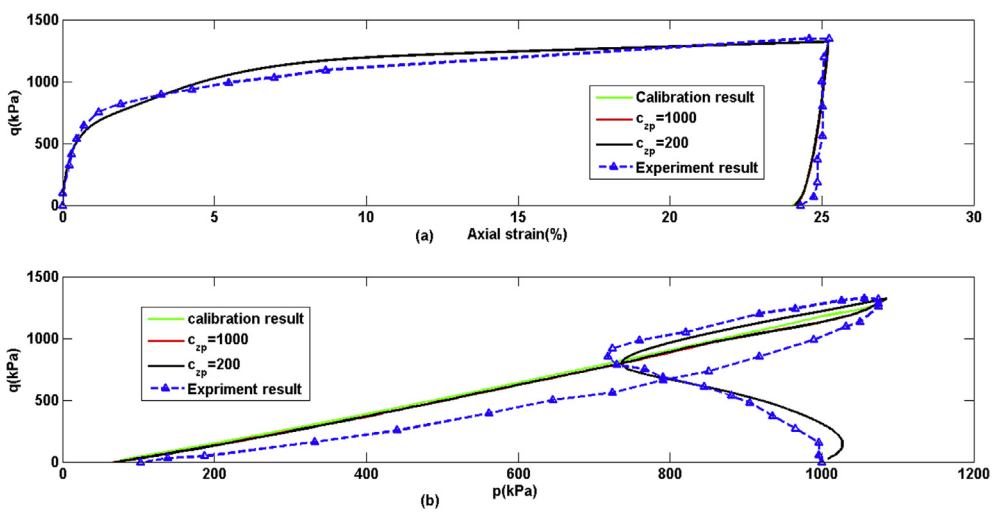

Fig. 9. The effects of constant C_{ZP} on the curves of the axial strain-deviatoric stress (a) and the confining pressure-deviatoric stress (b).

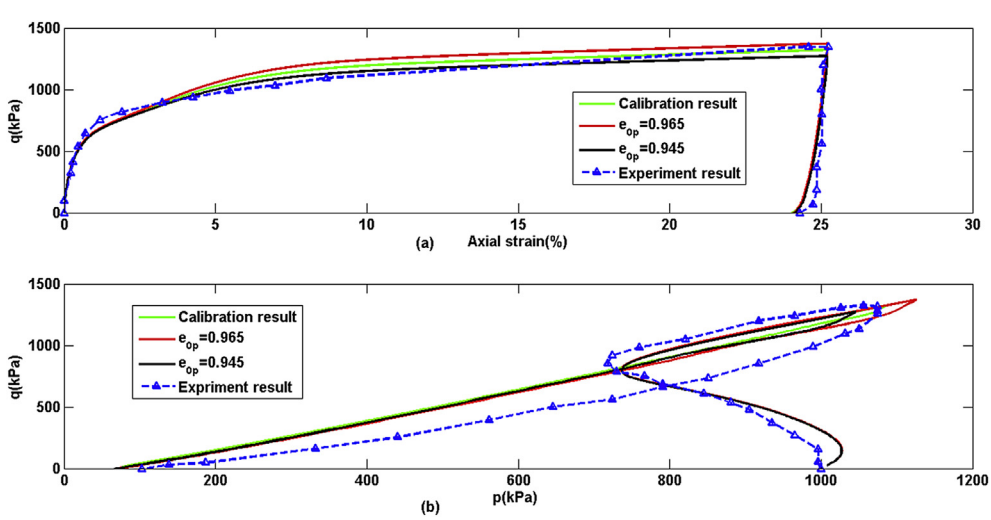

Fig. 10. The effects of constant e_{0P} on the curves of the axial strain-deviatoric stress (a) and the confining pressure-deviatoric stress (b).

experience a lower changes. By contrast, in the other plane constants, such as A_{0P}, n_{bP}, and n_{dP}, the changes that occur reflect lower effects on the behavioral curves of the different planes. An interesting point from the comparison of Figs. 6–20 is that unlike fabric constants C_{ZP} and Z_{maxP}, the constants do not exert an effect on soil behavior under loading but pose low effects on such behavior under unloading conditions. Given that the multilaminate framework can predict soil behavior in different directions, future research can examine the sensitivity of the

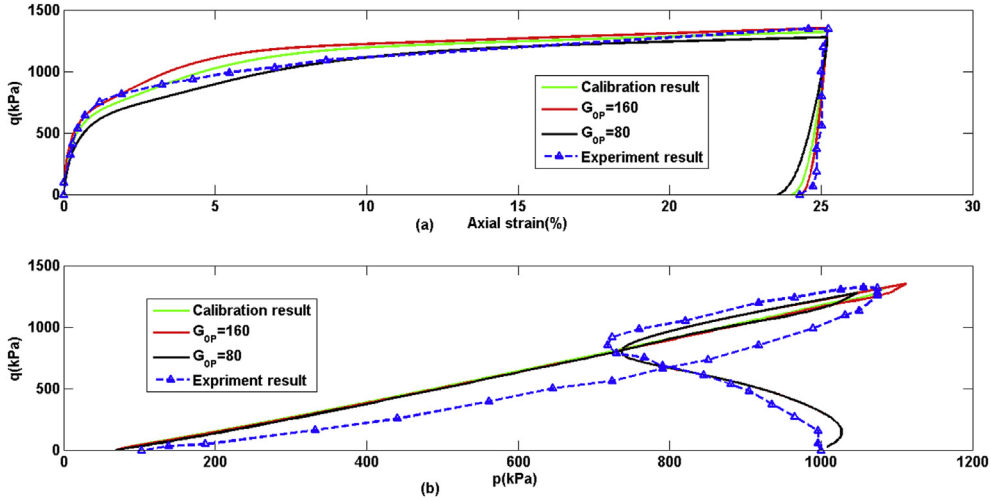

Fig. 11. The effects of constantG_{0P} on the curves of the axial strain-deviatoric stress (a) and the confining pressure-deviatoric stress (b).

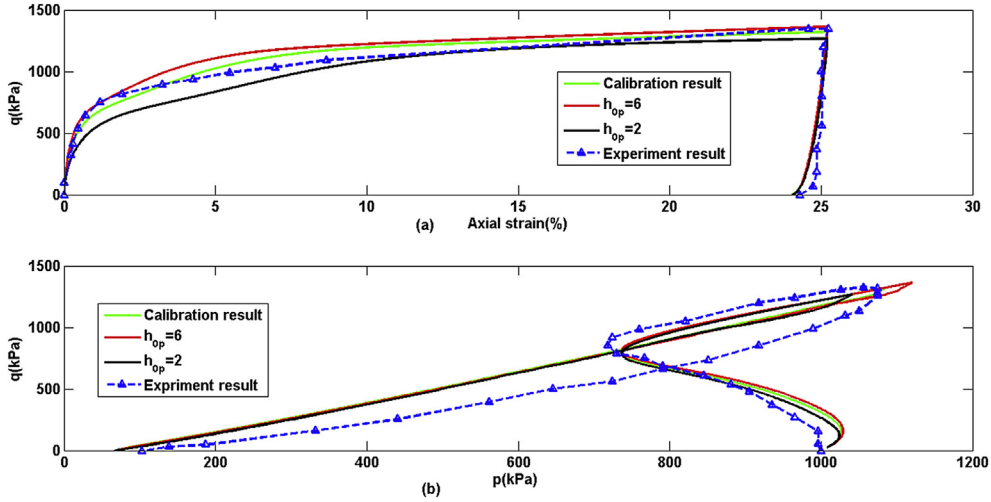

Fig. 12. The effects of constant h_{0P} on the curves of the axial strain-deviatoric stress (a) and the confining pressure-deviatoric stress (b).

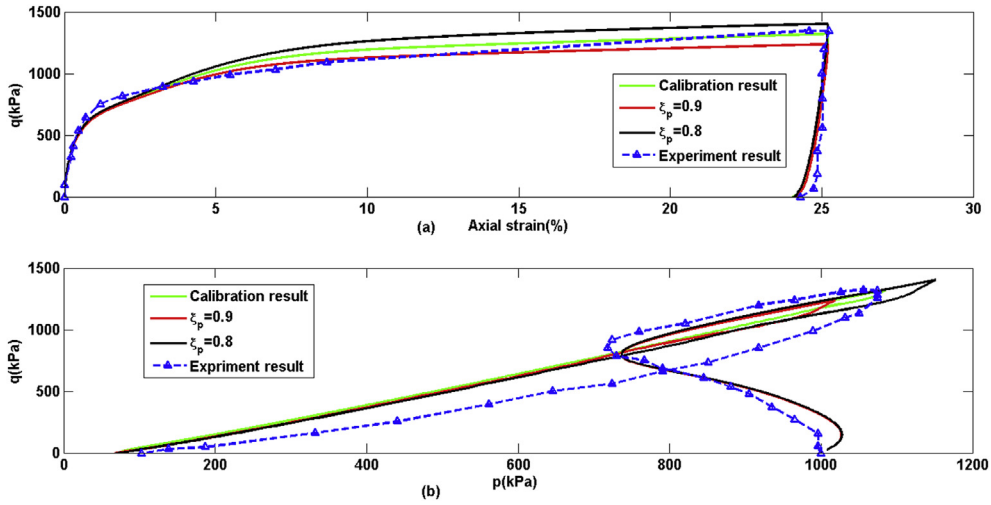

Fig. 13. The effects of constant ξ_P on the curves of the axial strain-deviatoric stress (a) and the confining pressure-deviatoric stress (b).

constants on the planes under loading and unloading, cyclic and monotonic, and drained and undrained conditions, as a result some of the constants can be removed from the equation used in the present work, and the simpler model that results from the removal can be more effective than the original model. For simplicity's sake, the initial behavior of the sand is assumed to be isotropic.

To compare the results of the numerical model with the experimental data, the pressure and void ratio of this model are assumed to be

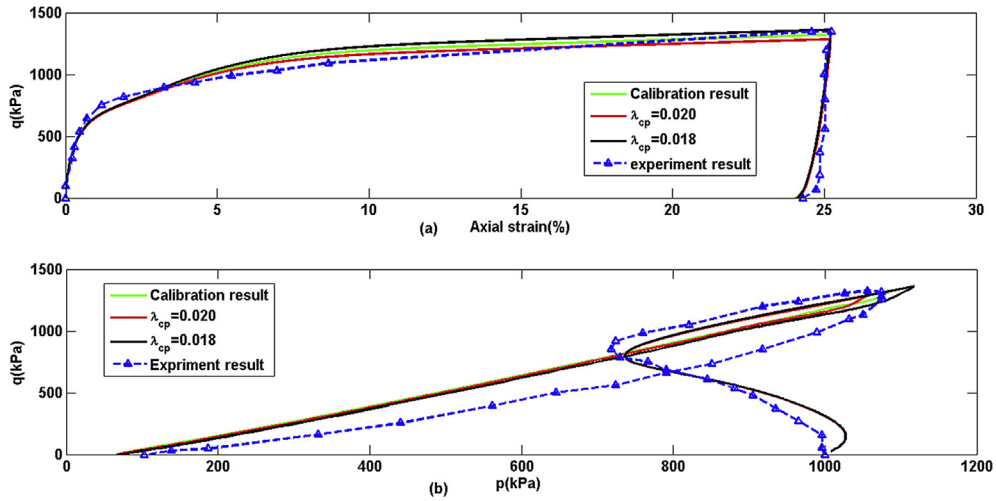

Fig. 14. The effects of constant λ_{cP} on the curves of the axial strain-deviatoric stress (a) and the confining pressure-deviatoric stress (b).

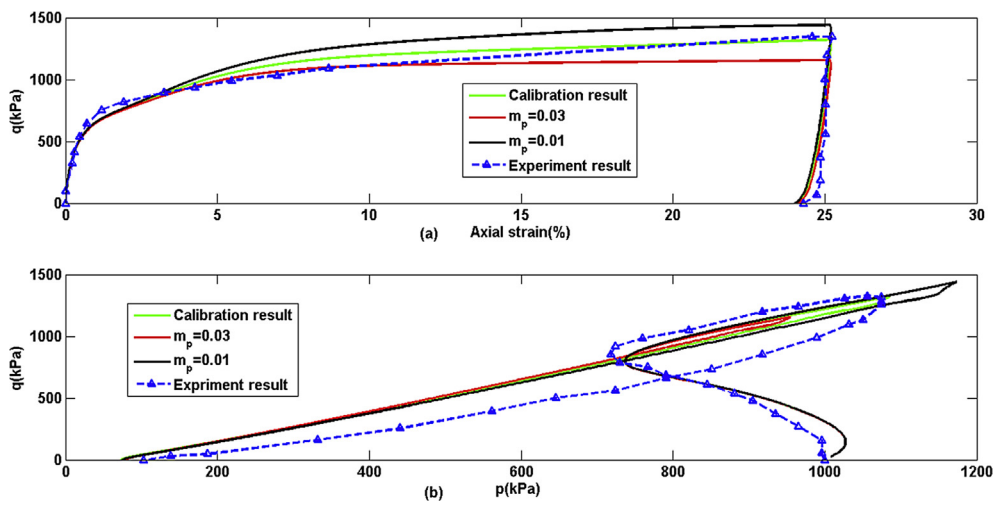

Fig. 15. The effects of constantm_P on the curves of the axial strain-deviatoric stress (a) and the confining pressure-deviatoric stress (b).

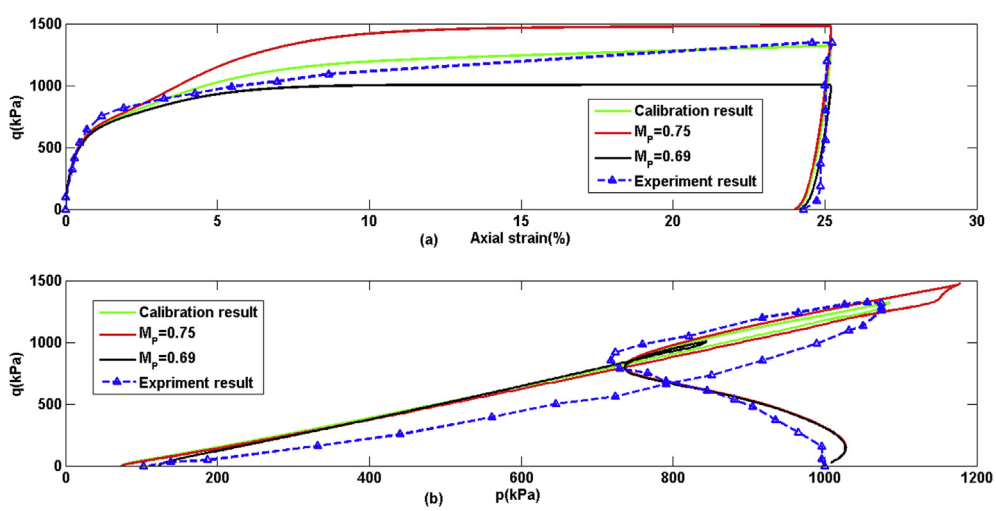

Fig. 16. The effects of constant M_P on the curves of the axial strain-deviatoric stress (a) and the confining pressure-deviatoric stress (b).

the average values of the entire range of their variations, i.e., $p_0 = 1000\ kPa$ and $e_0 = 0.833$ (Fig. 5). Considering the creation of excess pore pressure in the undrained condition, and its impact on the curves, the consistency of the results are checked with the results of the sample with the undrained condition. The resulting values of the plane constants are summarized in Table 2.

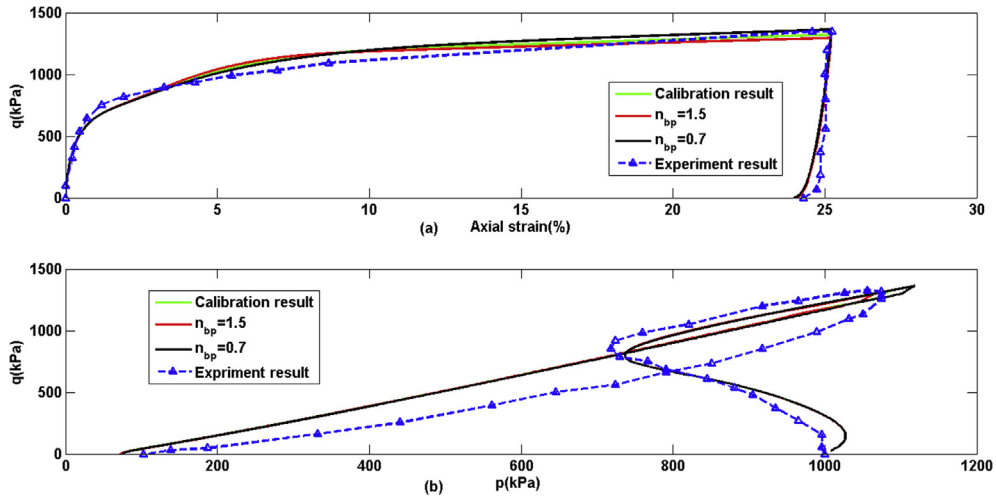

Fig. 17. The effects of constant n_{bP} on the curves of the axial strain-deviatoric stress (a) and the confining pressure-deviatoric stress (b).

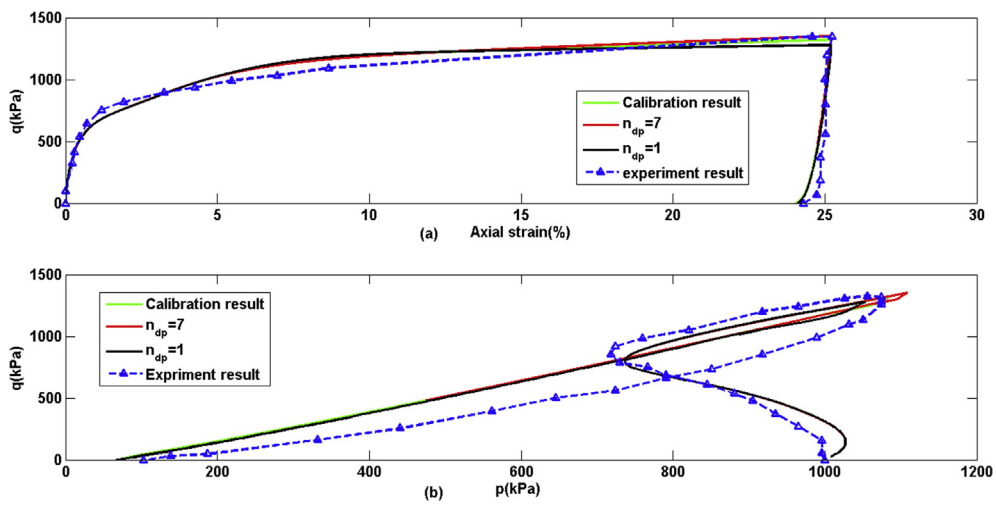

Fig. 18. The effects of constant n_{dP} on the curves of the axial strain-deviatoric stress (a) and the confining pressure-deviatoric stress (b).

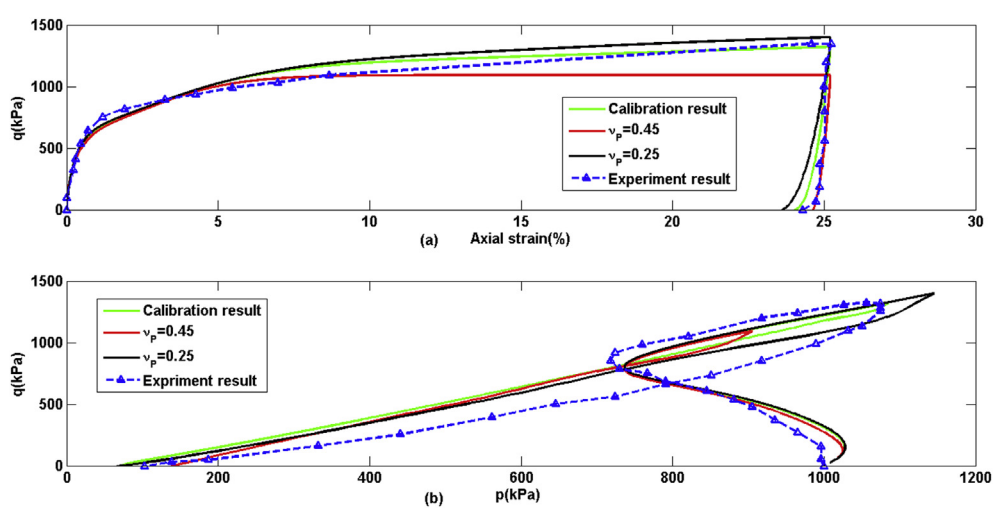

Fig. 19. The effects of constant ν_P on the curves of the axial strain-deviatoric stress (a) and the confining pressure-deviatoric stress (b).

5. Simulation and comparison

The experimental results of the standard triaxial tests conducted by Verdugo and Ishihara [43] under the drained and undrained conditions are used to check the simulation power of the multilaminate constitutive model.

Considering the extensive variations of confining pressure, ranging from 100 kPa to 3000 kPa, and the variations in the void ratio, ranging

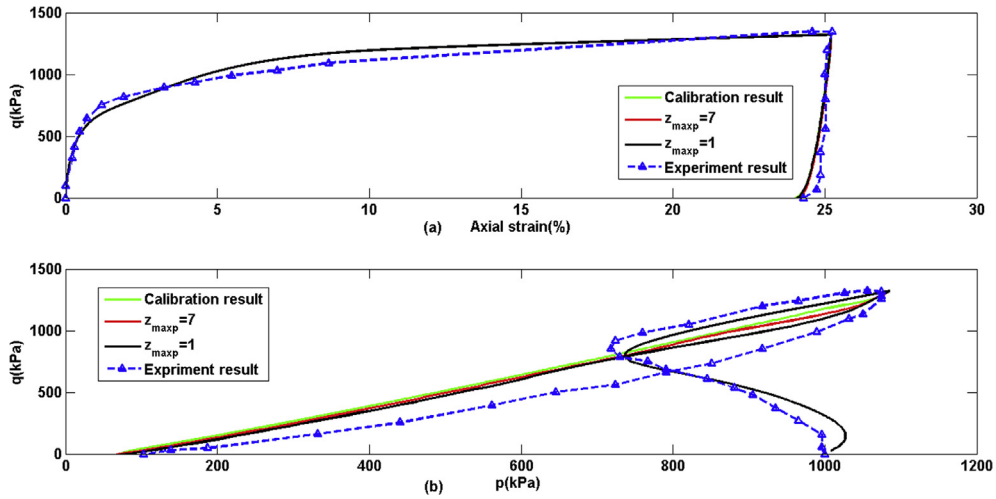

Fig. 20. The effects of constant z_{maxP} on the curves of the axial strain-deviatoric stress (a) and the confining pressure-deviatoric stress (b).

Table 2
Values of the plane constants.

Constant	Parameter	Value
Elasticity	G_{0P}	120
	ν_P	0.35
Critical State	M_P	0.72
	C_P	0.93
	λ_{cP}	0.019
	e_{0P}	0.955
	ξ_P	0.85
Yield Surface	m_P	0.02
Plastic Modulus	h_{0P}	4
	C_{hP}	1
	n_{bP}	1.1
Dilatancy	A_{0P}	0.5
	n_{dP}	4
Fabric	Z_{maxP}	4
	C_{ZP}	600

from 0.734 to 0.907, the results are evaluated under various conditions in terms of void ratio and confining pressure (Figs. 21–26). The softening behavior in high confining pressures is also well modeled.

Fig. 21 compares the path of deviatoric stress and shear strain obtained by the multilaminate model, and the experimental test for $p_0 = 100\,kPa$ and different e_0 values under the drained condition. In Fig. 22, the same comparison is made for $p_0 = 500\,kPa$. The high level of agreement between the simulation results and the experimental data demonstrates the model's good ability to accurately predict the softening behavior of dense sand. In Fig. 23, the simulation and experimental results are compared for $e_0 = 0.735$ and the different confining pressures under the undrained condition. The notable point in this figure is the sharper slope of the p-q curve in lower pressures ($p_0 = 100\,kPa$), which is consistent with theoretical predictions regarding the increase in the internal friction angle in soil in lower pressures and its decrease in higher pressures. Fig. 24 shows the simulation results obtained by adjusting the model constant for $e_0 = 0.735$; the results demonstrate a better agreement with the experimental results. Fig. 25 shows the model's good ability to simulate loose sand with a void ratio of $e_0 = 0.907$ during liquefaction. The unloading process due to kinematic hardening in inverse loading is also evaluated for both the drained and undrained conditions. Finally, Fig. 26 shows the model's ability to simulate the results for cyclic loading. The ability to predict inverse loading in the planes, and its effect at the point, is a major feature of this multilaminate model. The differences in the results of the cyclic conditions may be due to the fact that the cyclic tests were conducted 20 years before the monotonic tests; thus, this may lead to some differences in the methods used for the sample preparation, the instrument, etc. [24].

As can be seen, the good agreement between the multilaminate model results and the experimental results in most conditions demonstrates its good capability in these types of simulations.

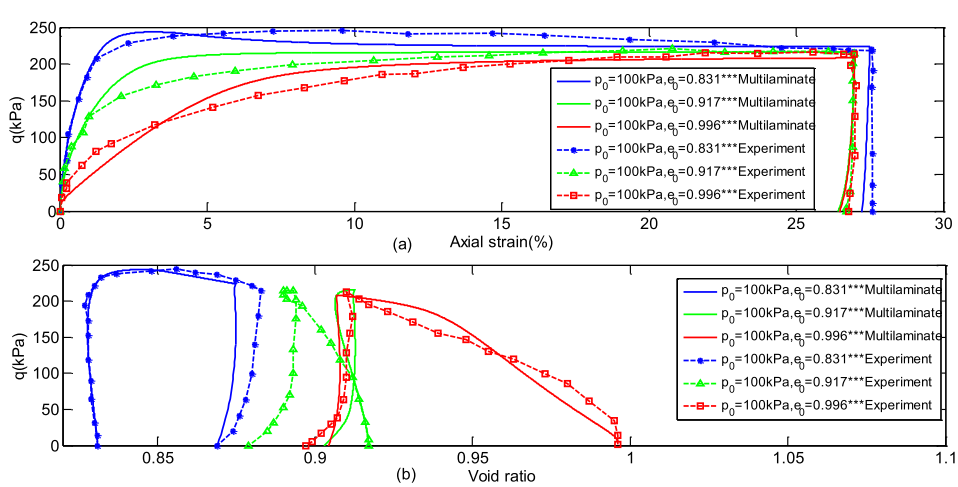

Fig. 21. Comparsion of the multilaminate and experimental results for monotonic loading and unloading in drained conditions in the standard triaxial test with $p_0 = 100\,kPa$; a) axial strain versus deviatoric stress; b) void ratio versus deviatoric stress.

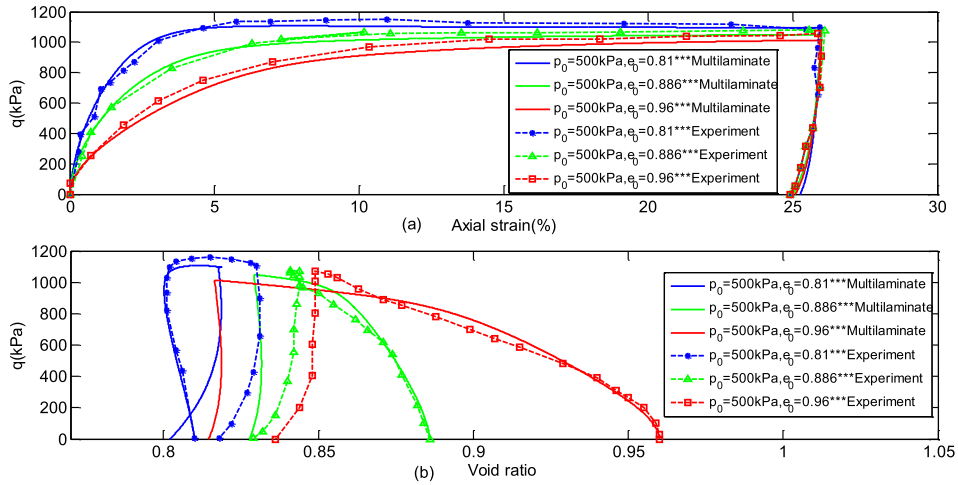

Fig. 22. Comparsion of the multilaminate and experimental results for monotonic loading and unloading in drained conditions in the standard triaxial test with $p_0 = 500\ kPa$; a) axial strain versus deviatoric stress; b) void ratio versus deviatoric stress.

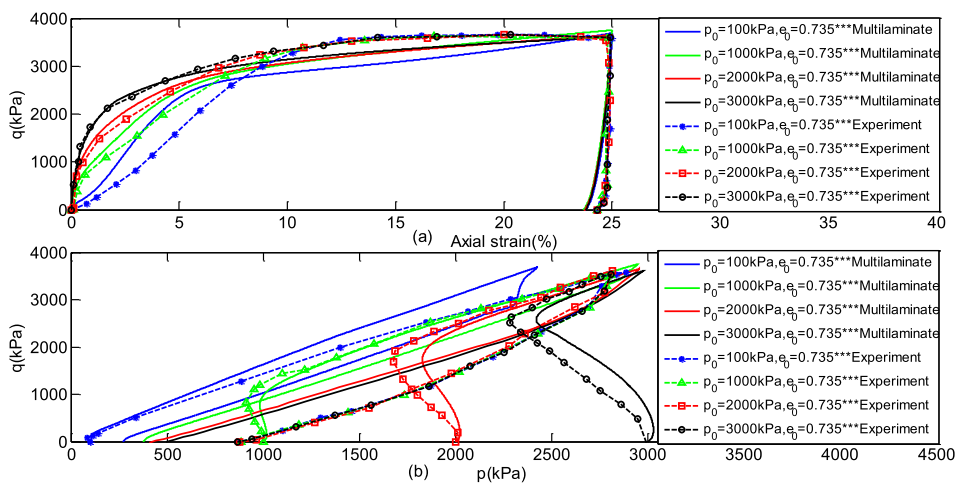

Fig. 23. Comparsion of the multilaminate and experimental results for monotonic loading and unloading in undrained conditions in the triaxial test with $e_0 = 0.735$; a) axial strain versus deviatoric stress; b)confining pressure versus deviatoric stress.

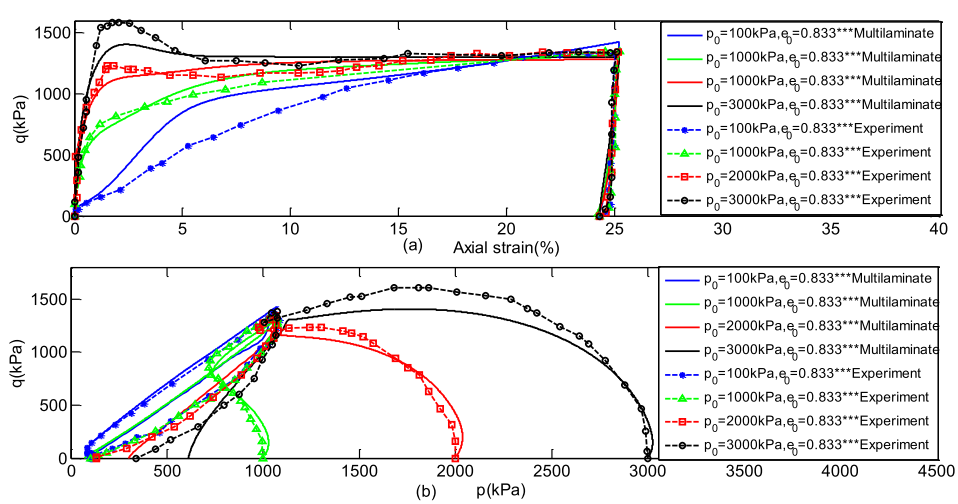

Fig. 24. Comparsion of the multilaminate and experimental results for monotonic loading and unloading in undrained conditions in the triaxial test with $e_0 = 0.833$; a) axial strain versus deviatoric stress; b)confining pressure versus deviatoric stress.

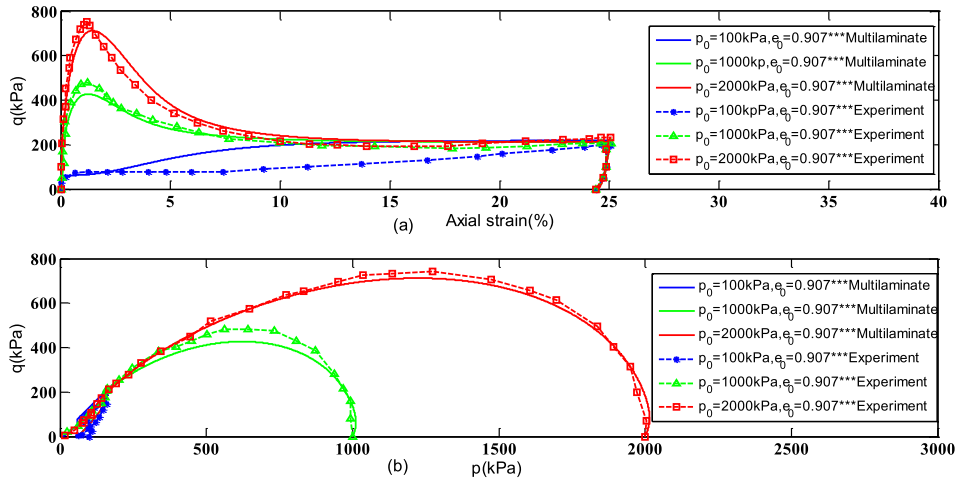

Fig. 25. Comparsion of the multilaminate and experimental results for monotonic loading and unloading in undrained conditions in the triaxial test with $e_0 = 0.907$; a) axial strain versus deviatoric stress; b)confining pressure versus deviatoric stress.

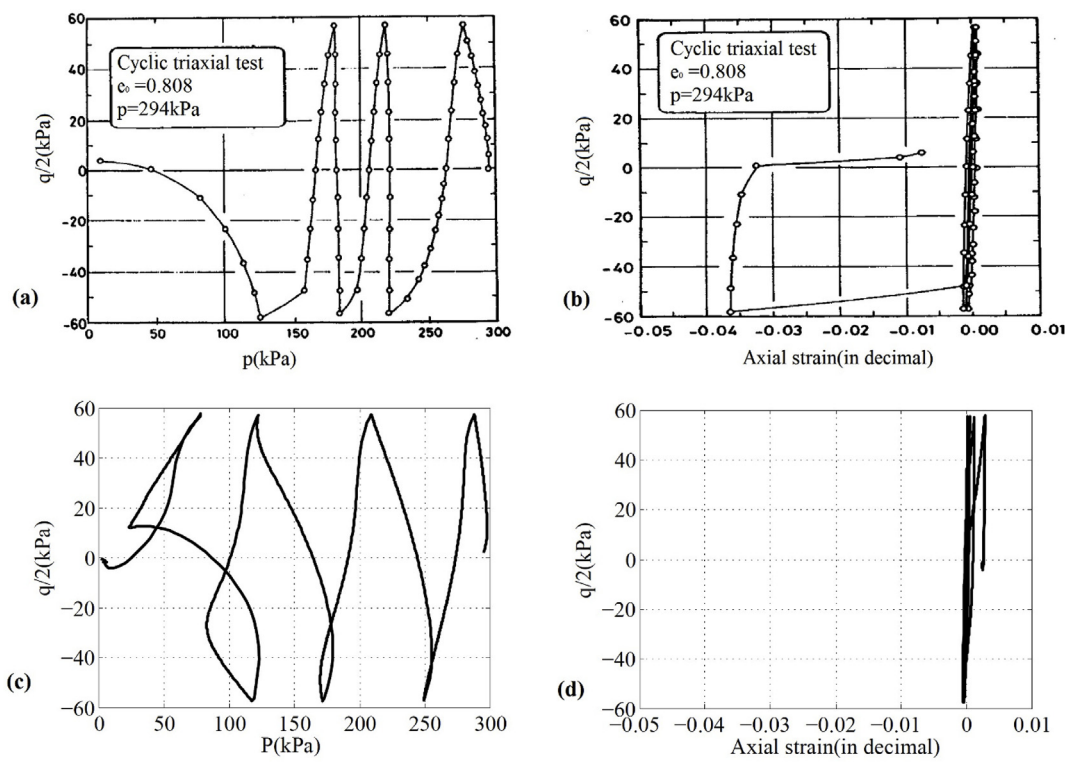

Fig. 26. Comparison of multilaminate (c,d), and experimental (a,b) results [24] for cyclic loading and unloading condition in undrained standard triaxial test with $p_0 = 294kPa$ and $e_0 = 0.808$

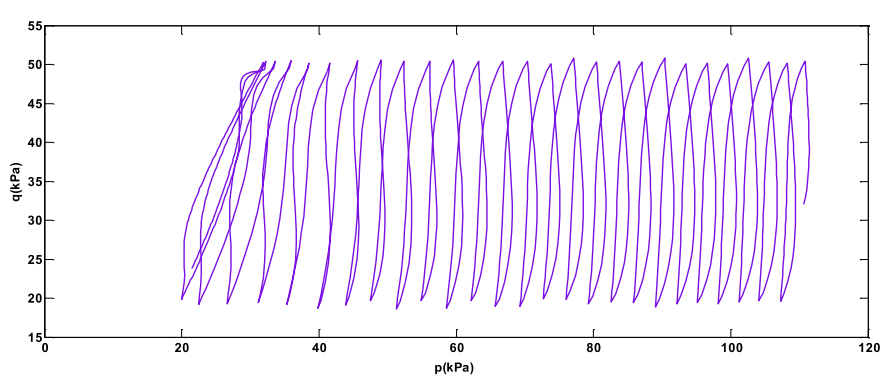

Fig. 27. Multilaminate modeling for cyclic loading standard triaxial test at $e_0 = 0.808$ and $\sigma_1 = 130kPa$, $\sigma_2 = \sigma_3 = 100kPa$, $q_{max} = 50kPa$, $q_{min} = 20kPa$

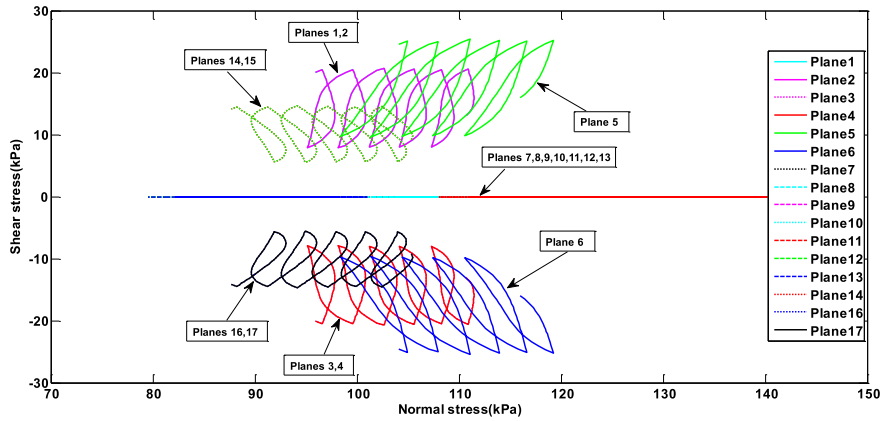

Fig. 28. The shear stress versus normal stress on 17 planes in cyclic undrained condition, with $e_0 = 0.808$ and $\sigma_1 = 130kPa,\ \sigma_2 = \sigma_3 = 100kPa,\ q_{max} = 50kPa,\ q_{min} = 20kPa$

To assess the effectiveness of the model under non-zero shear stress in the specimens and cyclic loading in undrained conditions, the samples with $\sigma_1 = 100$ kPa and σ_2, $\sigma_3 = 130$ kPa are selected. Cyclic loadings of q_max = 50 kPa and q_min = 20 kPa are applied until failure occurs in the soil samples. Fig. 27 illustrates the results of the imposition of different stress paths on the 17 planes (Fig. 28) in point. As shown in Fig. 28, the stress paths on some planes (e.g., planes 1 and 2 or 3 and 4) are similar, whereas those in other planes (e.g., planes 5 and 6) are different only in their direction. On planes 7 to 13, shear stress does not occur. The various stress paths cause different strains in different directions during loading—a result that confirms the effectiveness of the model in predicting induced anisotropy during loading.

6. Conclusion

The effects of inherent and induced anisotropies at the start of liquefaction and after the change in the shear behavior of sand highlight the need for an advanced model to simulate the behavior of sand. The presence of inherent anisotropy in the formation of sandy sediments and the development of shear-induced plastic deformations during loading and unloading, which leads to further anisotropy and local concentration of stress and strain, can cause local liquefaction, instability in the sand mass, and the development of a sliding surface along the weaker directions.

This study aimed to develop a way to more effectively assess anisotropy and strain and stress distributions, and examine their history in cohesionless soil in different conditions, such as liquefaction. To achieve this goal, instead of defining all the direction-dependent events on the three orthogonal planes using the Cartesian coordinate system, numerical integration was utilized to make use of 17 planes with predefined directions. This approach led to a more accurate and powerful assessment of anisotropy and its effects. The mentioned numerical integration has 17 reference points at the positions where the surface of the hemisphere with a negligible radius meets the vector that is normal to a plane tangent to that surface; in this way, the surface of the hemisphere was approximated with a 17-sided polyhedron. Development of stress and strain at a point leads to their development over the surface of the hemisphere; the value of the stress and strain are then averaged on the defined planes, the weight of each plane is then applied to the results, which are then transferred to the global coordinate system for integration to obtain the ultimate stress and strain. According to this method, the nonlinear behavior of the material at one point is the result of the numerical integration of the nonlinear behavior over the 17 planes. This method is able to reflect any behavioral changes in any of the planes in the form of opening-closing and sliding in both directions in the behavioral matrix of the point.

As was observed in this study, the use of the advanced Dafalias-Manzari model with 17 planes based on the multilaminate technique provided features, such as compatibility with the limit state of the soil, the definition of variable bounding and dilatancy surfaces, and the ability to predict the contractive and dilative behavior of sand and its softening behavior. Finally, the model's performance in predicting induced anisotropy is verified under non-zero shear stress and cyclic loading on the 17 planes.

The ability of the multilaminate model to predict the behavior of sand in drained and undrained conditions under cyclic loading allows different behavioral conditions to be incorporated into the new model. With this framework, the effects of constitutive differences during loading or unloading and the process of the development of plastic strains can be accurately predicted. These features enable the inherent and induced anisotropies to be properly incorporated into the constitutive model in order to address different initial conditions and loadings.

The structure of the model developed with the multilaminate framework provides the basis for the rotation of the principal axes and the noncoaxiality of the principal stresses and strains, and it allows for the effect of any small change in the boundary conditions to be reflected in the material's overall behavior while preserving the direction-dependent effects. This model also enables researchers to examine the condition of the formation of plastic strain under confining pressure. Further investigation of these features and other capabilities of the model are good subjects for future research.

References

[1] Yang ZX, Li XS, Yang J. Quatifying and modeling fabric anisotropy of granular soils. Geotechnique 2008;58(4):237–48.
[2] Guo N, Zhao J. The signature of shear-induced anisotropy in granular media. Comput Geotech 2013;47:1–15.
[3] Dafalias YF, Papadimitriou AG, Li XS. Sand plasticity model accounting for inherent fabric anisotropy. J Eng Mech 2004;130(11):1319–33.
[4] Yu H, Zeng X, Li B, Ming H. Effect fabric anisotropy on liquefaction of sand. J Geotech Geoenviron 2013;39:765–74.
[5] Tang Tron Tran H, Wong H, Dubujet Ph, Doanh T. Simulating the effects of induced anisotropy on liquefaction potential using a new constitutive model. Int J Numer Anal Met 2014;38(10):1013–35.
[6] Lashkari A. A constitutive model for sand liquefaction under rotational shear. Iran J Sci Technol 2009;33:31–48.
[7] Ye B, Ye G, Zang F. Numerical modeling of changes in anisotropy during liquefaction using a generalized constitutive model. Comput Geotech 2012;42:62–72.
[8] Gao Z, Zhao J, Li XS, Dafalias YF. A critical state sand plasticity model accounting for fabric evolution. Int J Numer Anal Met 2014;38(4):370–90.
[9] Zhao J, Guo N. Unique critical state characteristics in granular media considering fabric anisotropy. Geotechnique 2013;63(8):695–704.
[10] Lashkari A. A SANISAND model with anisotropic elasticity. Soil Dynam Earthq Eng 2010;30:1462–77.
[11] Yang ZX, Yang J, Wang LZ. Micro-scale modeling of anisotropy effects on undrained behavior of granular soils. Granul Matter 2013;15:557–72.
[12] Hicher PY, Chang CS. A microstructural elastoplastic model for unsaturated granular materials. Int J Solids Struct 2007;44:2304–23.

[13] Kruyt NP, Rothenburg L. A micromechanical study of dilatancy of granular materials. J Mech Phys Solids 2016;95:411–27.
[14] Khalili Y, Mahboubi A. Discrete simulation and micromechanical analysis of two-dimensional saturated granular media. Particuology 2014;15:38–150.
[15] Kruyt NP, Rothenburg L. On micromechanical characteristics of the critical state of two-dimensional granular materials. Acta Mech 2014;225:2301–18.
[16] Guo P. Coupled effects of capillary suction and fabric on the strength of moist granular materials. Acta Mech 2014;225:2261–75.
[17] Li X, Yu HS. Fabric, force and strength anisotropies in granular materials: a micromechanical insight. Acta Mech 2014;225:2345–62.
[18] Zhang JM, Wang G. Large post-liquefaction deformation of sand, part I: physical mechanism, constitutive description and numerical algorithm. Acta Geotech 2012;7:69–113.
[19] Wang G, Xie Y. Modified bounding surface hypoplasticity model for sands under cyclic loading. J Eng Mech 2014;140:91–101.
[20] Li XS. A sand model with state dependent dilatancy. Geotechnique 2002;52(3):173–86.
[21] Yang Z, Elgamal A. Multi-surface cyclic plasticity sand model with Lode angle effect. Geotech Geol Eng 2008;26:335–48.
[22] Andrianopoulos KI, Papadimitriou AG, Bouckovalas GD. Bounding surface plasticity model for the seismic liquefaction analysis of geostructures. Soil Dynam Earthq Eng 2010;30:895–911.
[23] Li XS, Ming HY. Unified modeling of flow liquefaction and cyclic mobility. Soil Dynam Earthq Eng 2000;19:363–9.
[24] Dafalias YF, Manzari MT. Simple plasticity sand model accounting for fabric change effects. J Eng Mech 2004;130:622–34.
[25] Wang R, Zang JM, Wang G. A unified plasticity model for large post-liquefaction shear deformation of sand. Comput Geotech 2014;59:54–66.
[26] Manzari MT, Dafalias YF. A critical state two-surface plasticity model for sands. Geotechnique 1997;47(2):255–72.
[27] Dafalias YF. Bounding surface plasticity. I: mathematical foundation and hypoplasticity. J Eng Mech 2000;112(9):966–87.
[28] Wang ZL, Dafalias YF, Shen CK. Bounding surface hypoplasticity model for sand. J Eng Mech 1990;116(5):983–1001.
[29] Taiebat T, Dafalias YF. SANISAND: simple anisotropic sand plasticity model. Int J Numer Anal Met 2008;32:915–48.
[30] Taiebat M. Advanced elastic-plastic constitutive and numerical modeling in geomechanics PhD thesis Davis: University of California; 2008
[31] Sadrnejad SA, Daryan AS, Ziaei M. A constitutive model for multi-line simulation of granular material behavior using multi-plane pattern. J Comput Sci 2009;5(11):822–30.
[32] Sadrnejad SA, Karimpour H. Drained and undrained sand behaviour by multi-laminate bounding surface model. Int J Civ Eng 2011;9(2):111–25.
[33] Khorami Fard G, Rasoolan I. Soil–pile interaction analysis using multi-laminate elasto-plastic modelling. Geotech Geol Eng 2017;35(4):1665–83.
[34] Sadrnejad SA. Semi-micro bounding surface model for anisotropic sand. Electron J Geotech Eng 2009;14:1–25.
[35] Ghadrdan M, Sadrnejad SA. Numerical evaluation of geomaterials behavior upon multiplane damage model. Comput Geotech 2015;68:1–7.
[36] Sadrnejad SA, Labibzadeh M. A continuum/discontinuum micro plane damage model for concrete. Int J Civ Eng 2006;4(4):296–313.
[37] Bazant ZP, Xiang Y, Adley MD, Prat PC, Akers SA. Microplane model for concrete: II: data delocalization and verification. J Eng Mech 1996;122(3):255–62.
[38] Caner FC, Bazant ZP. Microplane model M4 for concrete. II: algorithm and calibration. J Eng Mech 2000;126(9):954–61.
[39] Sadrnejad SA. Soil plasticity and modeling. 2th ed. Tehran: Khajeh Nasir Toosi University of Technology; 2011.
[40] Naylor DJ. Stresses in nearly incompressible materials by finite elements with application to the calculation of excess pore pressures. Int J Numer Methods Eng 1974;8(3):443–60.
[41] Tam HK. Some applications of cam-clay in numerical analysis PhD thesis City University London; 2008
[42] Taiebat M, Jeremic B, Dafalias YF, Kaynia AM, Cheng Z. Propagation of seismic waves through liquefied soils. Soil Dynam Earthq Eng 2010;30:236–57.
[43] Verdugo R, Ishihara K. The steady state of sandy soils. Soils Found 1996;36(2):81–91.